OPEN ACCESS

Enhancement of Performance and Sulfur Tolerance of Ceria-Based Fuel Electrodes in Low Temperature SOFC

To cite this article: F. Kullmann *et al* 2024 *J. Electrochem. Soc.* **171** 044511

Journal of The Electrochemical Society, 2024 **171** 044511

Enhancement of Performance and Sulfur Tolerance of Ceria-Based Fuel Electrodes in Low Temperature SOFC

F. Kullmann,[1,z] A. Schwiers,[2,3] M. Juckel,[2] N. H. Menzler,[2,3,*] and A. Weber[1,*]

[1]*Institute for Applied Materials (IAM-ET), Karlsruhe Institute of Technology (KIT), D-76131 Karlsruhe, Germany*
[2]*Forschungszentrum Jülich GmbH, Institute of Energy and Climate Research (IEK), IEK-1: Materials Synthesis and Processing, D-52425 Jülich, Germany*
[3]*RWTH Aachen University, Institute for Mineral Engineering (GHI), D-52074 Aachen, Germany*

The trend of operating the solid oxide fuel cell at significantly lower operation temperatures enables the application of electrodes with finer microstructure or even nanostructured electrodes with increased active surface and enhanced performance. To maintain the high performance in hydrocarbon fuels commonly impurified with sulfur compounds, a required sulfur tolerance has to be maintained. In this study we compare performance and H_2S-poisoning of four ceria-based electrodes: conventional $Ni/Ce_{0.9}Gd_{0.1}O_{2-\delta}$ cermets and sub-μm scaled $Ce_{0.8}Gd_{0.2}O_{2-\delta}$-electrodes with and without infiltrated nickel. Symmetrical cells were operated in a hydrogen/steam/nitrogen gas mixture with and without minor amounts of H_2S at 600 °C. The performance is analyzed by electrochemical impedance spectroscopy. The distribution of relaxation times is applied to deconvolute the electrochemical processes followed by a complex nonlinear least square fit to quantify the loss processes and the impact of sulfur. Whereas two different $Ni/Ce_{0.9}Gd_{0.1}O_{2-\delta}$ cermet electrodes exhibit polarization resistances at 600 °C without/with 0.1 ppm H_2S of 2.89/5.56 Ωcm^2 and 2.15/2.75 Ωcm^2, the single phase $Ce_{0.8}Gd_{0.2}O_{2-\delta}$ electrode reaches 0.98/2.37 Ωcm^2. With an infiltration of Ni-nitrate forming nickel nanoparticles on the gadolinia-doped ceria-surfaces, the *ASR* could be drastically reduced to 0.32/0.37 Ωcm^2.
 [DOI: 10.1149/1945-7111/ad3ebd]

Manuscript submitted January 31, 2024; revised manuscript received April 3, 2024. Published April 26, 2024. *This paper is part of the JES Focus Issue on SOFC XVIII: Advances in Solid Oxide Fuel Cell and Electrolysis Cell Technology.*

One of the major advantages of a solid oxide fuel cell (SOFC) is the high fuel flexibility.[1] Next to pure hydrogen, hydrocarbon fuels such as natural gas, propane or biogas can be utilized. Using hydrocarbon fuels, small amounts of impurities like sulfur are present in the fuel gas even if a desulfurizer unit is used. The remaining sulfur concentration, predominantly H_2S,[2] ranges between 0.1 ppm and 10 ppm (desulfurizer failure).[3] Previous studies[4–8] showed that the polarization resistance (ASR_{pol}) of the well-established Ni/YSZ (yttria-stabilized zirconia, YSZ) cermet anode in an anode-supported cell is strongly affected by sulfur at temperatures above 700 °C. This is assumed to be due to a hindered hydrogen electrooxidation at the triple phase boundary (TPB). Nickel acting in the Ni/YSZ fuel electrode as the only electrocatalyst for the hydrogen electrooxidation is blocked by a chemisorption of sulfur on the active nickel surface and TPB. As a result, adsorption and oxidation of hydrogen or surface transport are strongly impeded.[6,9–12]

Ni/GDC (gadolinia-doped ceria, GDC) fuel electrodes exhibit a much better sulfur tolerance at intermediate and high operating temperatures (750 to 850 °C)[5,13–16] and the poisoning is under some conditions even reversible.[3,16–18] The reason for this higher sulfur tolerance is related to the mixed ionic electronic conductivity of GDC arising from the different oxidation states of ceria (Ce^{3+} and Ce^{4+}) and the possibility for the electrooxidation to take place on the GDC-surface.[19–21] To our knowledge the exact reason for the higher sulfur tolerance is not clear. The most common explanations are an oxidation of adsorbed sulfur on the TPB/ceria surface where sulfur reacts to SO_2[13,22–24] followed by a reaction to H_2S with H_2[13] and a diffusion of sulfur into the GDC phase.[25–28]

The trend of operating SOFC-systems at a much lower temperature even below 600 °C[29,30] enables the application of nanostructured electrodes with high performance and durability.[31–33]

Previous studies revealed that an infiltration of nickel/ceria (forming nanoparticles during annealing) leads to a significant increase in performance and/or sulfur tolerance compared to a pure Ni/GDC cermet,[5,24,34,35] single phase GDC[23,34,36,37] or Ni/YSZ[5,38,39] fuel electrodes without infiltration. Primdahl et al.[37] compared the performance of GDC fuel electrodes sintered on an 8YSZ substrate with and without nickel infiltration between 700 and 1000 °C and observed a significant improvement of the GDC fuel electrode with Ni-infiltration especially at lower operation temperatures. The used current collector layer consisted of a composite of Au and GDC. Two processes in the impedance spectrum were detected. The lower frequency process was assigned to hydrogen adsorption and/or dissociation on the GDC surface whereas the higher frequency process was allocated to the ionic conductivity in the GDC electrode. Mirfakhraei et al.[23] also compared GDC electrodes with and without infiltrated Ni in a half-cell setup contacted with an Au current collector. The cells were operated in a 20 ml min^{-1} (H_2 + 3% H_2O) + 5 ml min^{-1} N_2 atmosphere between 500 and 800 °C and poisoned in H_2S containing atmosphere. The comparison of the performance supports the result of Primdahl et al.,[37] an improvement of performance by infiltrating nickel. In both studies[23,37] the Ni solely act as an electrocatalyst not as an electronic transport path. The impact of 10 ppm H_2S on the performance was also reduced by the infiltrated nickel. Two reasons for the improved sulfur tolerance were given.[23] Ni could act as a "sulfur adsorber" and is able to remove the sulfur from the GDC surface. Another explanation could be a higher steam production due to the nickel particles which improves the removal of sulfur from the surface.

In our previous work,[5,35] we compared the performance and sulfur tolerance of different infiltrations in Ni/GDC and Ni/YSZ cermet fuel electrodes at 750 °C in a $H_2/H_2O/N_2$ gas mixture corresponding to a typical composition of a simulated diesel reformate, with CO replaced by H_2 and CO_2 by H_2O. The infiltration of CeO_2 and/or Ni resulted in a significant increase in performance and sulfur tolerance. The improvement of the infiltrated electrodes was explained by an increased number of three phase boundaries in comparison to a rather coarse microstructure of the cermet.

Hays et al.[24] showed that in a hydrogen/methane atmosphere with 20 ppm H_2S a Ni/GDC cermet became nonfunctional after 70 h and the Ni/GDC with infiltrated GDC could be operated over 290 h in a stable mode at 650 °C. The difference in performance loss was explained by carbon deposition as well as sulfur adsorption. The GDC nanoparticles increase the number of reaction sites and are according to[24] able to provide oxygen ions by enhanced ion transport

*Electrochemical Society Member.
[z]E-mail: felix.kullmann@kit.edu

to the surface to form SO_2 and CO_2 leading to a decreased deposition/poisoning.

In this study four different fuel electrodes varying in their electrode design are investigated. The electrodes include Ni/$Ce_{0.9}Gd_{0.1}O_{2-\delta}$ cermet electrodes and single phase $Ce_{0.8}Gd_{0.2}O_{2-\delta}$ fuel electrodes with and without infiltrated Ni and Ni current collector layer. The symmetrical cells are operated in the similar model fuel[5,35] at 600 °C and are analysed by electrochemical impedance spectroscopy (EIS) before, during and after sulfur poisoning. For a quantitative analysis the distribution of relaxations times (DRT)[40] is used to deconvolute the peaks in the impedance spectrum followed by a complex nonlinear least square (CNLS) fit.[41] An equivalent circuit model was applied to quantify the loss processes and to compare the performance and sulfur tolerance.

Experimental

The experimental cells are symmetrical electrolyte-supported cells with an active area of 1 cm^2. The approximately 200 μm thick electrolyte consists of 8 mol% yttria-stabilized zirconia (8YSZ). To investigate the impact of the electrode design on the performance and sulfur tolerance four different fuel electrodes are applied. Table I shows the manufacturing parameters and the setup of the cells and Fig. 1 includes the scanning electron microscopy (SEM) cross sections. For this post-test analysis cross section images of the cells were recorded by a Zeiss 1540 XB. The imaging was performed with an accelerating voltage of 1.3 kV and a SE2 detector. As the Ni-contact layer is not sintered on the (Ni/)GDC-layer, it is detached from the electrode during dismounting the cells from the test bench after testing and is therefore not visible in the cross sections in Fig. 1.

Figures 1a, 1b show the cross sections of two types of Ni/$Ce_{0.9}Gd_{0.1}O_{2-\delta}$ fuel electrodes with 10 mol% of gadolinia-doped ceria. In Fig. 1a the Ni/GDC10 layer is directly screen printed on the 8YSZ substrate (sample A). The screen-printing paste was prepared at Forschungszentrum Jülich GmbH. In Fig. 1b a GDC10-layer is applied between electrolyte and fuel electrode with an additional screen-printed and not sintered NiO-contact layer on top (sample B, manufactured at Forschungszentrum Jülich GmbH). With these additional layers and the reduced sintering time the sample represents an improved fuel electrode design compared to sample A. The layer thicknesses and sintering procedures are listed in Table I.

Figures 1c–1f show the cross sections of two cells with an identically manufactured GDC-layer. Both sides of the electrolyte are screen printed with a 20 mol% gadolinia-doped ceria ($Ce_{0.8}Gd_{0.2}O_{2-\delta}$, GDC20) layer (sample C/D). The screen-printing paste was developed at Forschungszentrum Jülich GmbH, Germany. The sintering temperature of the GDC20 layer is with 1200 °C lower than the sintering temperature of the GDC10 interlayer of sample B, since the purpose of the layer is different. In sample C/D the layer functions as an electrochemically active layer where a finer microstructure is more favorable. The GDC10 layer in sample B should be denser since it should simply function as a barrier layer to avoid direct contact of NiO and 8YSZ during sintering. The electrodes of sample D were infiltrated by Ni-nitrate solution forming Ni-nanoparticles on the internal GDC20 surfaces after annealing and reduction pictured in Figs. 1d, 1f. To visualize the difference in microstructure Figs. 1e, 1f shows a cutout of Figs. 1c, 1d with a higher magnification. The infiltration was performed in vacuum at ambient temperature with a water based solution of 46 wt% $Ni(NO_3)_2 \cdot 6\ H_2O$. After drying the cells at 70 °C the $Ni(NO_3)_2$ was calcined at 400 °C. Since the electronic conductivity of GDC is orders of magnitude below that of Ni-based cermet electrodes, a screen-printed NiO layer was applied as current collector. The contact layer was dried at 70 °C in ambient air and reduced during testing at 800 °C to Ni.

The test setups used in this study are described in Refs. 42 and 43 For contacting the fuel electrodes nickel meshes were applied. The cell was located in one gas chamber and the total flow was 500 sccm. The gas mixture consists of 25% H_2, 25% H_2O and 50% N_2 and the temperature is 600 °C. The gas mixture was chosen similar to previous studies[5,35] and simulates a model diesel reformate with CO replaced by H_2 and CO_2 by H_2O. CO and CO_2 were avoided to prevent additional effects due to sulfur-related deactivation of the water gas shift reaction.[6,44,45] The sulfur content was varied between 0.1 ppm and 1.0 ppm H_2S. The low amount of 0.1 ppm, which is still in the range of sulfur contents in real desulfurized hydrocarbon fuel gases,[3] was chosen to decelerate the impact of sulfur over time recorded by impedance spectra. With higher amounts of sulfur in the fuel gas, the measurement time of one impedance spectrum takes longer than the poisoning effect on the electrode which leads to more difficult process assignment. Before the poisoning tests were started, the stability of all cells was checked by measuring impedance spectra for at least 10 h in a stable operation point.

After the reduction at 800 °C the samples A, C and D were operated at 700 °C in 50% H_2 and 50% H_2O until stabilization. For sample B a different starting procedure at 800 °C and 600 °C was used. The aim of the starting procedures is to reduce ageing in the subsequent investigation at 600 °C.

The EIS measurements were performed without bias current by a Solartron 1260 in galvanostatic mode. The value of the sinusoidal stimulus was chosen in order to receive a voltage response of the electrode of $\leqslant$ 12 mV.[42] The frequency ranges from 30 mHz to 1 MHz. To guarantee valid impedance spectra the linear Kramers Kronig validity test was used.[46,47] For the impedance data analysis DRT[40] and subsequent CNLS-fitting[41] were applied in order to separate and quantify the loss processes in the spectrum.[43]

Since the focus of this work is solely on the fuel electrode performance, the cell setup was not designed for an application in a full cell. With a 200 μm thick 8YSZ electrolyte an ohmic resistance of 1.82 $\Omega\ cm^2$ at 600 °C is to be expected and therefore the cell is not applicable for a technically meaningful application in a system. More promising cell concepts at this operation temperature range are fuel electrode supported or metal supported cells[29,30] where the electrolyte thickness and subsequently the ohmic resistance can strongly be reduced.

Table I. Manufacturing parameters and setup of the investigated samples.

Sample	A	B	C	D
active electrode	Ni/GDC10-cermet	Ni/GDC10-cermet on GDC10-layer	GDC20-layer	GDC20-layer + Ni-infiltration
contact layer	—	Ni (800 °C)	Ni (800 °C)	Ni (800 °C)
Ni/GDC layer	Ni/GDC10	Ni/GDC10	—	—
	− ~17 μm	− ~11 μm		
	− 1400 °C, 5 h	− 1400 °C, 3 h		
GDC layer	—	GDC10	GDC20	GDC20
		− ~6 μm	− ~5 μm	− ~5 μm
		− 1300 °C, 3 h	− 1200 °C, 3 h	− 1200 °C, 3 h
		+ 1400 °C, 3 h		+ Ni-infiltration
substrate	8YSZ	8YSZ	8YSZ	8YSZ

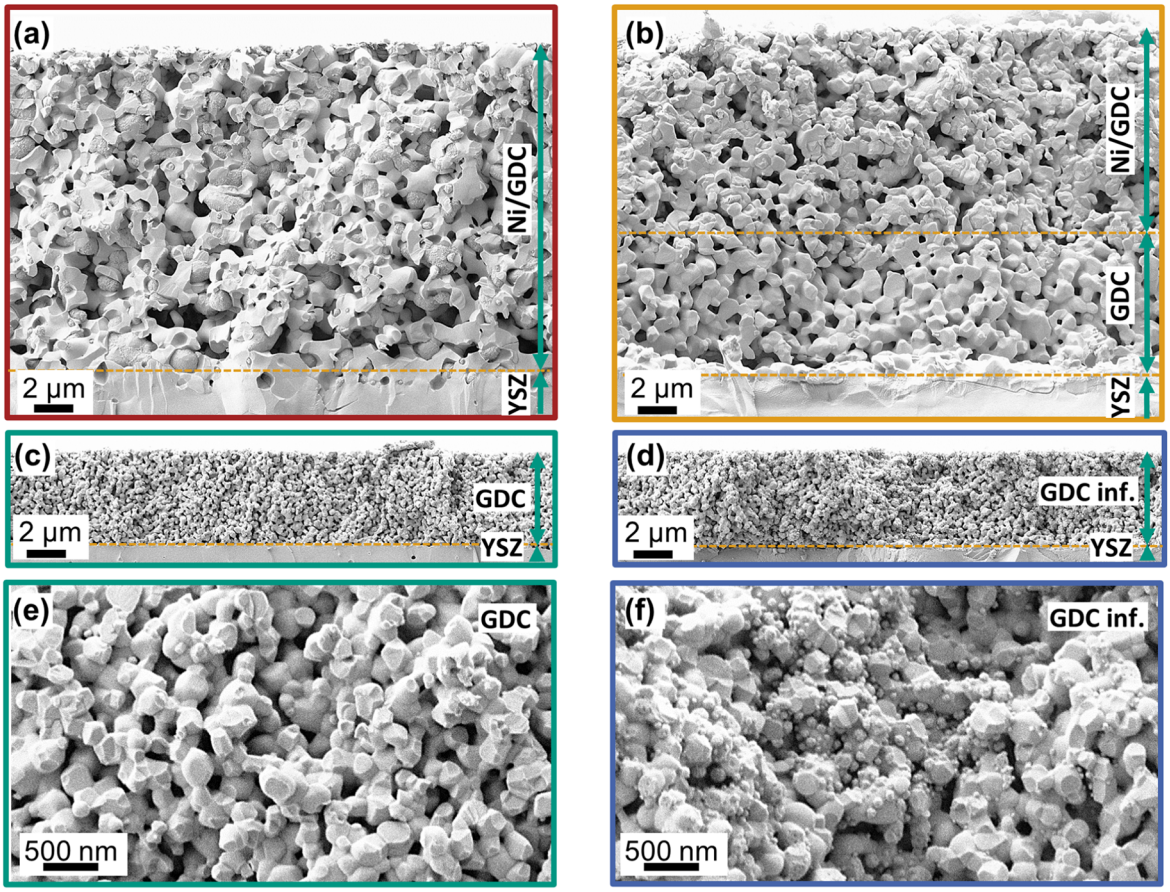

Figure 1. Scanning electron microscopy (SEM) cross section of symmetrical fuel electrode cells received by SE2 detector. (a) sample A, (b) sample B, (c, e) sample C and (d, f) sample D. (e, f) is a cutout of (c, d) with a higher magnification to visualize the infiltrated nickel. The images were taken from the post-test analysis of the cells. In all cases the Ni-contact layer sticked to the Ni-contact mesh and thus delaminated during removing the cell from the test bench.

Results and Discussion

A comparison of the impedance spectra/DRT of the two Ni/GDC10 fuel electrode cells and the two GDC20 fuel electrode cells is pictured in Fig. 2. All cells were operated at a stable operation point at 600 °C in 25%/25%/50% $H_2/H_2O/N_2$, for about ∼10 h. Figures 2a, 2b show the impedance/DRT of a Ni/GDC10 fuel electrode directly printed and sintered on the 8YSZ substrate. The DRT includes two low frequency peaks which are typically allocated to surface processes overlapping with gas diffusion (LF_1) and to the ionic transport in the GDC-phase (LF_2) respectively.[37,48–51] The impedance/DRT in Figs. 2c, 2d is recorded from a Ni/GDC10 fuel electrode not directly applied on the 8YSZ (sample B). An additional porous GDC10-layer is applied in between 8YSZ electrolyte and Ni/GDC10 fuel electrode (Fig. 1b). A comparison of the Nyquist plot of sample A and sample B shows an improvement of the ohmic resistance. This can be allocated to the additional Ni-contact layer which was applied on top of the Ni/GDC10 fuel electrode of sample B resulting in an improved current collection. Additionally, it is also well known that nickel diffuses from the electrode into the YSZ electrolyte during sintering and decreases the ionic conductivity of YSZ[52–54] resulting in an increased ohmic resistance. This could be the case for sample A as the Ni/GDC10 is directly applied on the YSZ. With an improvement of the ohmic resistance from 2.35 Ω cm^2 (sample A) to 1.78 Ω cm^2 (sample B) an excellent agreement with the expected resistance of the pristine 8YSZ-substrate of 1.82 Ω cm^2 is achieved. The resistance contributions are determined by fitting an equivalent circuit model to the impedance data consisting of one resistor for the ohmic resistance and one RQ-element for each fully recorded peak in the DRT revealing the polarization resistance. The beginning of the peak with a peak frequency above 1 MHz and therefore not fully recorded was also fitted by an RQ element and added to the ohmic resistance. As shown in Ref. 55 the ohmic contributions at high temperatures are expected to show an RC-polarization behavior caused by dielectric processes with a relaxation frequency of > 1 MHz for YSZ. This can't be resolved in the impedance spectrum due to limitation in frequency, but applying a significantly lower operation temperature shifts the processes to lower frequencies and inside the frequency range of the impedance analyzer and a RC-polarization behavior becomes visible.[55]

The DRT of sample B shows as in sample A mainly two low frequency peaks. In comparison to sample A the polarization resistance is decreased as expected from previous studies.[5,22,35,56] The reduced peak height of LF_1 and the frequency shift towards higher frequencies indicates a decrease of the charge transfer resistance. The reason for this impact of the GDC10-interlayer is not fully understood at this point. There might be an activation of the GDC-surface in the interlayer or an improved charge transfer at the interface between 8YSZ and GDC. The higher polarization resistance of sample A could also be explained by a formation of porosity at the interface between electrode and electrolyte which can be prevented by the application of a GDC interlayer.[56] It has also to be considered that the activation of the complete electrode through the Ni-contact layer might improve the electrode performance.

Figures 2e, 2f show the impedance spectra and the DRT of a symmetrical cell with a single phase GDC20-layer followed by a Ni-contact layer between GDC20-layer and nickel mesh labeled as sample C. The Ni-contact layer is necessary for any cell without a continuous Ni-phase in the electrode to guarantee a sufficient in-

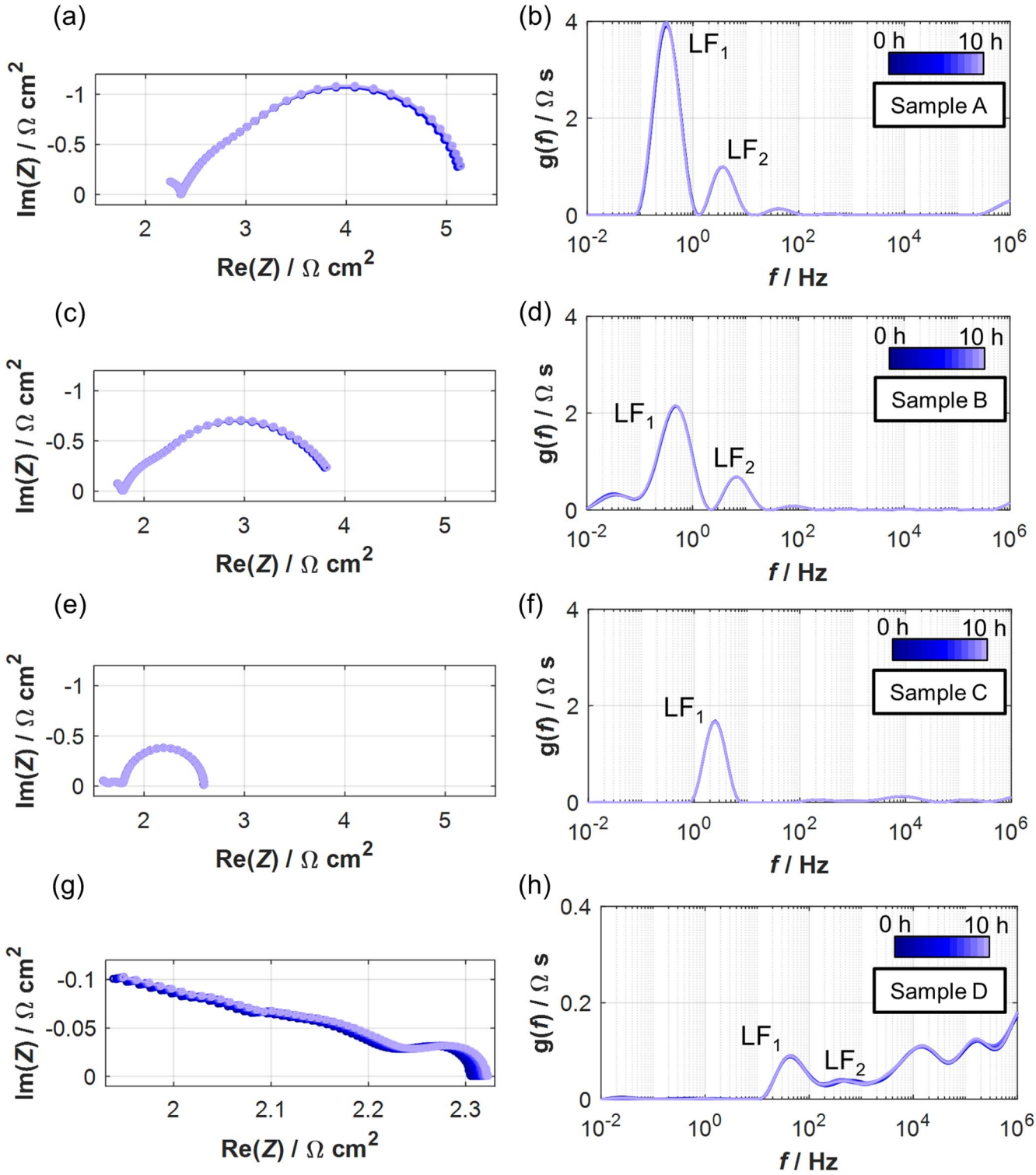

Figure 2. Impedance spectra (Nyquist plot on the left-hand side and DRT on the right-hand side) at a stable operation point (∼10 h after reduction) at 600 °C in 25%/25%/50% $H_2/H_2O/N_2$. (a, b) sample A, (c, d) sample B, (e, f) sample C, (g, h) sample D. (g, h) is scaled down by a factor of 10 (EIS: Im, Re, DRT: g(f)). The impedance measurements represent one electrode and half of the electrolyte resistance.

plane conductivity and a low contact resistance between GDC20-layer and nickel contact mesh. Pre-tests showed that without such contact layer a complete utilization of the 1 cm^2 active area of GDC20 is not possible due to insufficient in-plane conductivity of the GDC-layer.[57,58] Applying the Ni-contact layer leads to an ohmic resistance of 1.63 $\Omega \cdot cm^2$ which is even slightly below the expected resistance of the 8YSZ-substrate of 1.82 $\Omega \cdot cm^2$, proving a complete utilization of the cell area. The 5 μm thick GDC20 layer has no severe impact on the ohmic resistance. The DRT shows one major peak called LF_1 at ∼2.5 Hz. A few peaks with a much lower resistance are visible between 100 Hz and 1 MHz. According to our recent publication[51] LF_1 represents the charge transfer resistance plus minor gas diffusion losses whereas the higher frequencies peaks feature the bulk conductivities inside the GDC20 electrode and

interface between 8YSZ and GDC. The observed polarization resistance of sample C, which exhibits nominally pure GDC20 electrodes, is, with a value of 0.98 $\Omega \cdot cm^2$ (600 °C), much lower compared to previous GDC electrodes (137.6 $\Omega \cdot cm^2$, at 750 °C) analyzed in a Ni-free environment.[35] This difference can be attributed to the application of a current collector layer and the subsequent activation of the complete electrode. Also nickel from this contact layer might diffuse into the GDC20-layer during testing. A recent publication of our group showed a detection of small amounts of nickel inside the GDC layer in a similar cell setup.[59] Ni deposited on the GDC-surfaces in the porous GDC-layer will act as the electrocatalyst. In this case we talk about an activation of the GDC surface or the DPB since there are no visible Ni-particles within the resolution of the SEM.[51]

Figures 2g, 2h show the impedance at 600 °C of the identically manufactured GDC20-layer with infiltrated nickel (sample D). In this setup a Ni-contact layer is used, too. The major difference in the impedance between sample C and D is the value of the polarization resistance and the relaxation frequency of peak LF_1. The resistance decreases and the frequency increases, which indicates an improvement of the charge transfer reaction. It should be noted that the axis in Figs. 2g, 2h are adjusted by a factor of 10. The difference regarding the surface reactions is demonstrated in a schematic drawing in Figs. 3c, 3d. The higher amount of TPBs/activation of the GDC surface due to nickel seems to lead to a drastic decrease in ASR_{LF1-2} of about one order of magnitude compared to sample C and to a shift in relaxation frequency to ~40 Hz. This improvement of the electrode performance can be supported by the research of Primdahl et al.[37] and Mirfakhraei et al.[23] which is explained by an additional enhanced reaction pathway between Ni-, ceria- and gas-phase which is next to the ceria/gas interface much faster. With the decrease of the peak height of LF_1 in sample D, processes at higher frequencies become more visible compared to sample C as the ionic conduction in the GDC-phase is not affected by the Ni-infiltration. As shown in Ref. 51 for the GDC20 fuel electrode, they are most probably related to ionic transport in the porous electrode (transmission line behavior) as well as interdiffusion and secondary phase formation at the GDC/YSZ-interface.[60] In sample D no clear separation of ASR_{ohm} and ASR_{pol} is possible in the Nyquist plot. Applying the same approach as for the other cells leads to an ohmic resistance of 2.00 $\Omega \cdot cm^2$ which is higher than the ASR_{ohm} of the non-infiltrated cell. This behavior could be confirmed by repeat measurements of identical cells. The reason for this is not clear. Nickel diffusion into the YSZ, decreases the ionic conductivity[52–54] usually at much higher temperatures during the sintering process.

Figure 4 shows the DRTs of the impedance spectra of all four different symmetrical cells operated at 600 °C in 25%/25%/50% $H_2/H_2O/N_2$. Since the resistance difference between the cells is hardly visible in a linear *y*-axis (a), in Fig. 4b a logarithmic y-scale is applied. The advantage of the presentation in logarithmic scale is that every peak in the DRT is visible even if there is a large difference in peak height as it is the case for sample C. But it has to be considered that the area under the peaks is no longer corresponding to the polarization resistance as in diagrams with linear y-scale. A comparison between the GDC20 fuel electrodes and the Ni/GDC10 cermet electrodes shows a much higher performance of the GDC20 fuel electrodes. The polarization contributions in the low frequency range are significantly reduced. This could have several reasons. One explanation is the increased active surface due to a larger volume specific GDC-surface area (sample C and D) and additionally an increased surface activity due to the coverage by nanoscaled Ni-particles (only sample D). In sample A and B, large Ni-particles, which are only active at the TPB but not on the entire Ni-surface, result in a large inactive surface area. In case of sample D, the whole Ni-surface of the nanoparticles is close to the TPB and thus, according to elementary kinetic modeling results,[61] contributing to the charge transfer reaction. In addition, the GDC20 fuel electrodes exhibit a finer microstructure compared to the Ni/GDC10 fuel electrodes due to lower sintering temperature, which increases

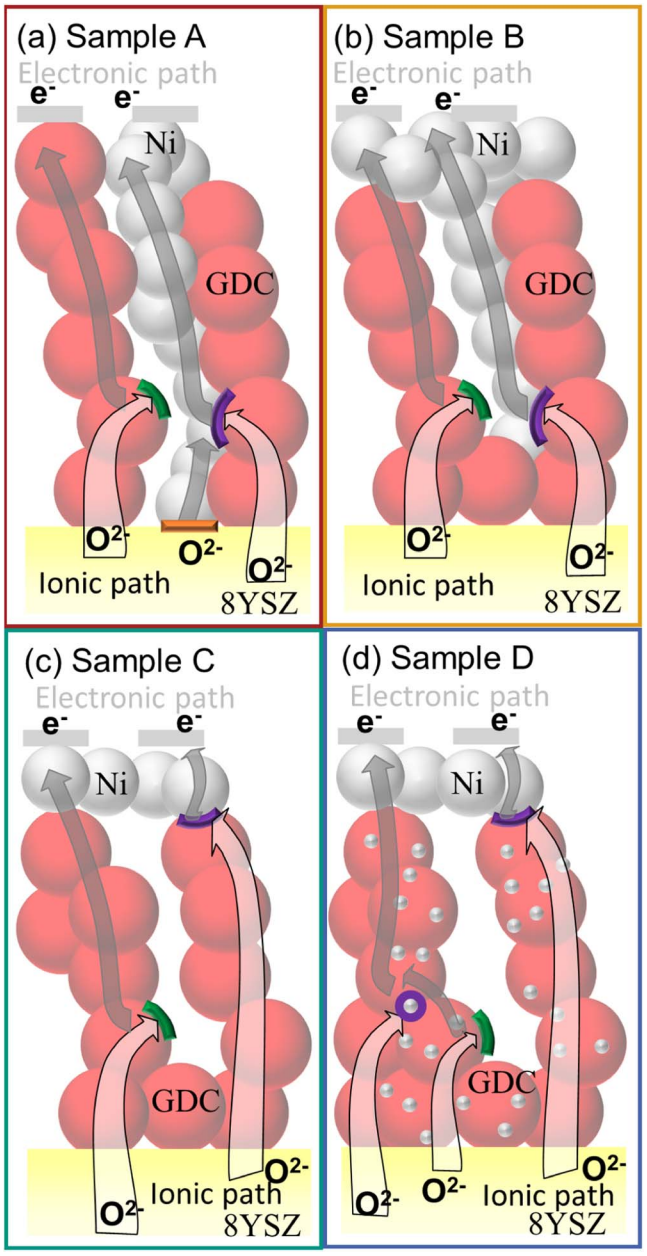

Figure 3. Schematic drawing of the electrochemistry of the investigated cells. The charge transfer at the double phase boundary (DPB) is colored in green, the reaction at the TPB between Ni, GDC and gas phase in purple and between Ni, YSZ and gas phase in orange. (a) sample A, (b) sample B, (c) sample C and (d) sample D.

the surface area.[62] It should be considered that the difference in the doping amount of gadolinia in ceria between 20 mol% in the GDC20 fuel electrodes and 10 mol% in the Ni/GDC10 cermet electrodes might lead to a minor influence as Riegraf et al. suggested.[17]

The peaks ($f > 100$ Hz) of the two cells with GDC20 fuel electrode (sample C, D) show comparable values (Fig. 4). The high frequency peaks of sample A and B are not comparable with the two GDC20 fuel electrodes since the sintering temperature and the batch of the substrate differ. The sintering temperature affects the interaction between YSZ and GDC strongly as shown in Ref. 63.

To study the difference in sulfur tolerance the four ceria-based fuel electrodes are operated at 600 °C in 25%/25%/50% $H_2/H_2O/N_2$ and poisoned with 0.1 ppm H_2S. The impedance spectra and DRTs are depicted in Fig. 5. The blue curves correspond to the sulfur free operation, which did not cause any degradation, and the red curves

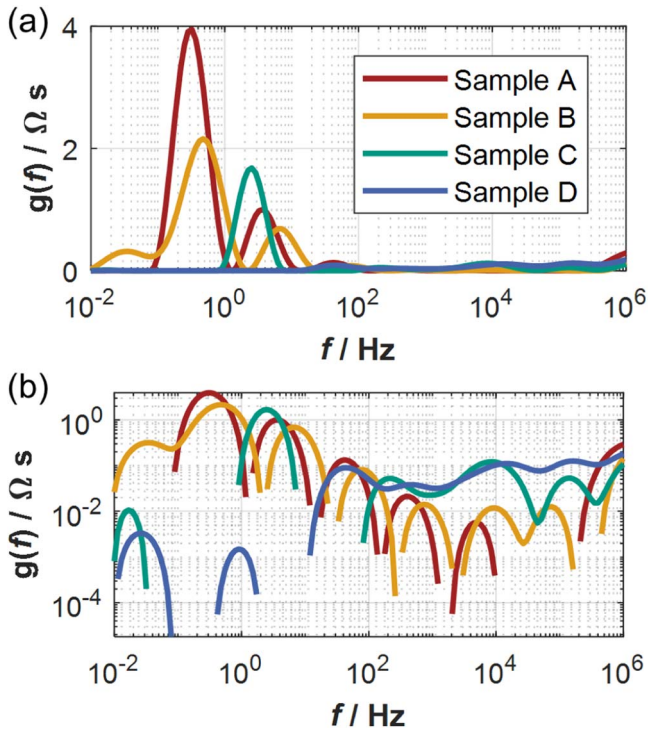

Figure 4. DRTs of impedance spectra measured at 600 °C in 25%/25%/50% $H_2/H_2O/N_2$ of the four different cells, (a) linear *y*-axis and (b) logarithmic y-scale. The DRTs corresponds to one electrode´s polarization resistance.

reveal the increase in polarization resistance during the sulfur poisoning phase. The Ni/GDC10 fuel electrode directly printed and sintered on an 8YSZ substrate (sample A) in Figs. 5a, 5b shows a large increase in polarization resistance of the peak LF_1 which underlines its assignment to surface processes.[5,16,64,65] The sulfur might affect the DPB between GDC and gas phase and/or the TPB between nickel, GDC and gas phase and hinders the electrooxidation of hydrogen as discussed above. LF_2 shows minor dependency as expected for a bulk process. The ohmic resistance remains constant. Since all the cells show negligible degradation at the same operation point without sulfur, we can assume that the degradation of the ASR_{pol} is exclusively caused by the sulfur poisoning.

The application of an additional GDC10-layer between the Ni/GDC10 and the 8YSZ electrolyte (sample B) in Figs. 5c, 5d decreases the impact of sulfur at 600 °C and is in accordance with the results obtained at higher operation temperatures.[5,22,35] In this case process LF_2 shows no dependency. The reason for the higher sulfur tolerance could be due to the missing Ni/YSZ TPBs. When applying Ni/GDC10 directly on 8YSZ we assume that the most active TPBs, which are located at the electrode/electrolyte interface, are between nickel, YSZ and gas phase[5] as pictured in Fig. 3a. Since the Ni/YSZ is more sensitive to sulfur than Ni/GDC[5,13,14,16] the GDC-layer in between reduces the impact of sulfur. Another explanation for the higher sulfur tolerance of sample B could be that the GDC interlayer provides a higher amount of oxygen ions at the interface between fuel electrode and interlayer to oxidize the chemisorbed sulfur and clean the most active part of the triple phase boundaries near the interface. A similar effect could be seen by Hays et al.[24] in a GDC infiltrated Ni/GDC fuel electrode where the GDC particles in a Ni/GDC fuel electrode significantly improved the sulfur tolerance. Furthermore, a diffusion of sulfur into the GDC[25–28] could clean the TPB at the interface and reduce the impact of sulfur on the electrode performance.

The strong increase of the lower frequency peak LF_1 of sample C in Figs. 5e, 5f is clearly visible whereas the higher frequency peaks and the ohmic resistance remain constant which is consistent with the previous process assignment. Figures 5g, 5h pictures the impedance evolution of the identically manufactured GDC20-layer with infiltrated nickel (sample D). Please consider that the axes (except for frequency) in Figs. 5g, 5h are adjusted by a factor of 10. When adding sulfur to the fuel gas, a small increase of LF_1 is visible and a minor change in LF_2 whereas the higher frequency peaks remain constant. This confirms the assignment of bulk processes which are independent of surface poisoning. For further improvement of the sulfur tolerance of sample D one could think about an additional GDC interlayer between infiltrated GDC layer and 8YSZ electrolyte. The realization of this approach would be challenging. If a GDC layer with a porosity comparable to sample B is applied, nickel will be infiltrated into this layer during the sample preparation as well. To get this interlayer denser a higher sintering temperature would be necessary leading to an enhanced interaction between YSZ and GDC[63] and increase the ohmic resistance. Another approach would be the application of a physical-vapor deposited GDC layer as in Ref. 66, but this approach would be out of the scope of this paper and would cause problems due to the high sintering temperature of the porous GDC20 electrode layer. Therefore, we decided to apply the fuel electrode in sample D directly on the 8YSZ electrolyte.

To quantify the losses and compare performance and sulfur tolerance more precisely a CNLS-fit is applied to an equivalent circuit model to fit the impedance measurements. For this fit a rather simple equivalent circuit model consisting of one resistor for the ohmic resistance and one RQ-element for each fully recorded peak was used. As for the unpoisoned analysis the beginning of the peak with a relaxation frequency above 1 MHz was also fitted by an RQ element and added to the ohmic resistance. It has to be mentioned that impedance measurements during poisoning do not completely satisfy the requirements for low Kramers Kronig residues,[46,47] since the time invariance due to sulfur poisoning is not given. This instability features a lower frequency peak in the DRT at 30 mHz and a break away at the lower frequency end in the Nyquist plot as shown for instance in Figs. 5e, 5f. It is explainable by the measurement time of the spectrum which takes longer than a measurable aging effect of the cell. This artificial low frequency peak was already reported in Ref. 67 for Ni/YSZ fuel electrodes.

To quantify the increase of the polarization resistance due to poisoning, the reference measurement before adding H_2S and after stabilizing the cell in poisoned condition should be evaluated.

In Fig. 6 the discussed difference between the cells in initial performance (open circles, $t < 0$ h) is clearly visible. An additional GDC10 layer between the Ni/GDC10 and the 8YSZ and the additional Ni contact layer improve the performance of the cell (sample A and B). Using a single phase GDC20-layer with a finer microstructure and a Ni-contact layer on top (sample C) the performance could be even more improved. With an infiltration of nickel (sample D) the ASR_{pol} of the GDC20 fuel electrode could be reduced by a factor of 3 compared to sample C.

At $t = 0$ h, 0.1 ppm H_2S is applied (filled circles, Fig. 6). After adding, it takes some time until the ASR_{pol} increases. This is most probably due to sulfur adsorption in the gas lines as well as in the Ni-contact layer. After this initial time the *ASR* values increase rapidly for any kind of cell. After a few hours a stable ASR_{pol} is reached. An improvement of the sulfur tolerance could be achieved by an additional GDC10 layer in the Ni/GDC10 fuel electrode, as already shown for higher operating temperatures in Refs. 5, 22, 35 The ASR_{pol} in sample A increases about 93% whereas the resistance of sample B increases only by 28%. Sample C seems to be less sulfur tolerant than sample B by an increase of about 142%, but nevertheless it has a higher performance in 0.1 ppm H_2S. The infiltrated GDC20 fuel electrode (sample D) comes even in the poisoned state with the highest performance of the investigated cells and shows only an increase in ASR_{pol} of about 16%. The *ASR* values for every cell are summarized in Table II.

Sample A and C were, after poisoning with 0.1 ppm H_2S, poisoned with 1 ppm H_2S (at $t = 24/26$ h, start visualized by arrows) which is followed by an additional increase of ASR_{pol}. The increase is much lower compared to the difference between 0 ppm and 0.1

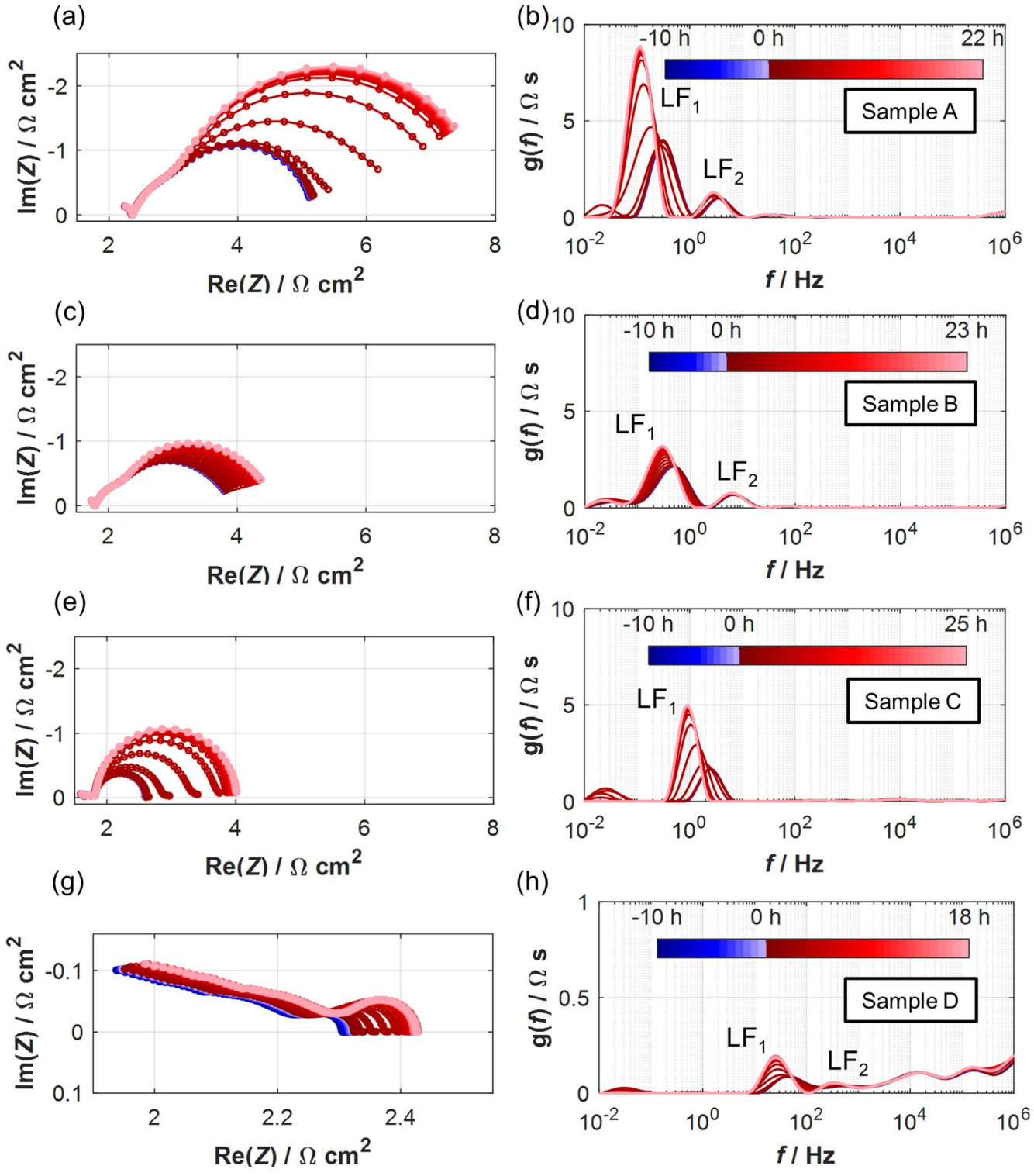

Figure 5. Impedance spectra (Nyquist plot on the left-hand side and DRT on the right-hand side) during sulfur poisoning with 0.1 ppm H_2S at 600 °C in 25%/25%/50% $H_2/H_2O/N_2$ featured in red (start at $t = 0$h) compared to reference measurements with no H_2S added in the fuel gas featured in blue. (a, b) Sample A, (c, d) Sample B, (e, f) Sample C and (g, h) Sample D. (g, h) is scaled down by a factor of 10 (EIS: Im, Re, DRT: g(f)). The impedance measurements show one electrode and half of the electrolyte resistance.

ppm H_2S. This was expected and is explainable by the surface coverage of nickel.[9] After applying this higher amount of sulfur a regeneration phase without sulfur was conducted. The regeneration of sample C seems to be better than for sample A, but this has to be further investigated since the regeneration time was too short to stabilize the *ASR*. Nevertheless, the time to regenerate would be to long for a useful technical application. But the almost complete regeneration is according to[7] an indication for a reversible adsorption of H_2S on the nickel catalyst without significant irreversible reactions or enhanced microstructural changes.

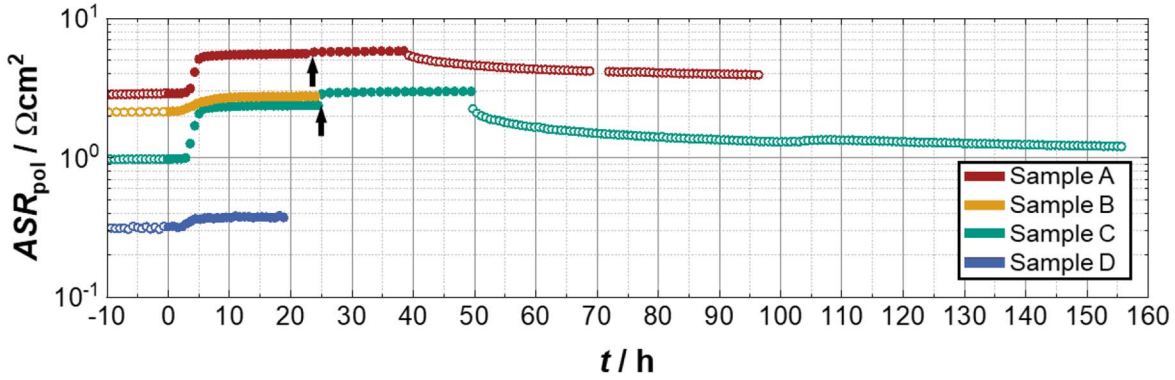

Figure 6. ASR_{pol} over time before, during and after sulfur poisoning at 600 °C in 25%/25%/50% $H_2/H_2O/N_2$. At $t = 0$ h 0.1 ppm H_2S is added to the fuel gas (fulfilled circles represent H_2S in the fuel gas). Operation without sulfur is represented by open circles. In case of samples A and C a higher amount of 1 ppm H_2S was used (start visualized by arrows) followed by a regeneration without H_2S.

Table II. *ASR* values of the investigated samples at 600 °C in Ω cm².

ASR value/Ω cm²	A	B	C	D
ASR_{ohm}	2.35	1.78	1.63	2.00
ASR_{pol}	2.89	2.15	0.98	0.32
ASR_{pol} (0.1 ppm H_2S)	5.56	2.75	2.37	0.37
ASR_{pol}(0.1 ppm H_2S)/ASR_{pol}	1.93	1.28	2.42	1.16

Conclusions

An enhancement of performance and sulfur tolerance of ceria-based fuel electrodes operated at 600 °C in a technically relevant model diesel reformate could be achieved by improving layer sequence and microstructure.

It is remarkable that electrodes consisting of a layer of GDC20 sintered at a temperature of 1200 °C and thus exhibit a rather large internal GDC-surface area show the best performance before and after sulfur poisoning. We assume that the GDC-surface in the pores of this layer is activated by nickel, diffusing from the Ni-contact layer (sample C) and which has been infiltrated (sample D), respectively. Even without infiltration ASR_{pol}-values of 0.98 Ω cm² (before poisoning) and 2.37 Ω cm² (poisoned state, 0.1 ppm H_2S) were achieved at 600 °C. The infiltration of nickel nitrate forming nanoparticles on the GDC surface resulted in a further drastic *ASR*-decrease. The *ASR* values were decreased to 0.32 Ω cm² and 0.37 Ω cm² in the non-poisoned and poisoned state, respectively. In case of the Ni/GDC10 electrodes with and without GDC10-interlayer higher *ASR*-values (2.15 Ω cm²/2.75 Ω cm² and 2.89 Ω cm²/5.56 Ω cm²) were obtained (values in non-poisoned/poisoned state, 0.1 ppm H_2S).

In the next step performance and impact of sulfur should be related to microstructural features of the layers as TPB-density, density of accessible GDC-surface area and Ni- electrocatalyst distribution in the GDC-layer.

Acknowledgments

We gratefully acknowledge funding from the German Federal Ministry of Education and Research (BMBF) within the WirLebenSOFC project No.: 03SF0622E and the German Science Foundation (DFG) via the SynSOFC 2 project. The authors thank Luis Salamon and Phillip Reichert for the assistance in the laboratory and Annette Schucker for taking the SEM images. Further acknowledgment is extended for the open access funding provided by the KIT Publication Fund of the Karlsruhe Institute of Technology, Germany.

ORCID

F. Kullmann https://orcid.org/0000-0002-6653-5601
N. H. Menzler https://orcid.org/0000-0001-7091-0980
A. Weber https://orcid.org/0000-0003-1744-3732

References

1. A. Weber, *Fuel Cells*, **21**, 440 (2021).
2. K. Sasaki, *J. Fuel Cell Sci. Technol.*, **5**, 031212 (2008).
3. E. Brightman, D. G. Ivey, D. J. L. Brett, and N. P. Brandon, *J. Power Sources*, **196**, 7182 (2011).
4. S. Dierickx, T. Mundloch, A. Weber, and E. Ivers-Tiffée, *ECS Trans.*, **78**, 1273 (2017).
5. A. Weber, S. Dierickx, N. Russner, and E. Ivers-Tiffée, *ECS Trans.*, **77**, 141 (2017).
6. A. Kromp, S. Dierickx, A. Leonide, A. Weber, and E. Ivers-Tiffée, *J. Electrochem. Soc.*, **159**, B597 (2012).
7. J. F. B. Rasmussen and A. Hagen, *J. Power Sources*, **191**, 534 (2009).
8. A. Hauch, A. Hagen, J. Hjelm, and T. Ramos, *J. Electrochem. Soc.*, **161**, F734 (2014).
9. J. B. Hansen, *Electrochem. Solid-State Lett.*, **11**, B178 (2008).
10. D. R. Huntley, *Surf. Sci.*, **240**, 13 (1990).
11. C. H. Bartholomew, *Appl. Catal. A: Gen.*, **212**, 17 (2001).
12. A. Kromp, *Model-based interpretation of the performance and degradation of reformate fueled solid oxide fuel cells*, Karlsruhe Institute of Technology (2013), KIT Scientific Publishing Karlsruhe.
13. S. Kavurucu Schubert, M. Kusnezoff, A. Michaelis, and S. I. Bredikhin, *J. Power Sources*, **217**, 364 (2012).
14. L. Zhang, S. P. Jiang, H. Q. He, X. Chen, J. Ma, and X. C. Song, *Int. J. Hydrog. Energy*, **35**, 12359 (2010).
15. M. Gong, X. Liu, J. Trembly, and C. Johnson, *J. Power Sources*, **168**, 289 (2007).
16. M. Riegraf, M. P. Hoerlein, R. Costa, G. Schiller, and K. A. Friedrich, *ACS Catal.*, **7**, 7760 (2017).
17. M. Riegraf, V. Yurkiv, R. Costa, G. Schiller, and K. A. Friedrich, *ChemSusChem*, **10**, 587 (2017).
18. P. Lohsoontorn, D. J. L. Brett, and N. P. Brandon, *J. Power Sources*, **183**, 232 (2008).
19. M. Mogensen, T. Lindegaard, U. R. Hansen, and G. Mogensen, *J. Electrochem. Soc.*, **141**, 2122 (1994).
20. M. Mogensen and J. J. Bentzen, *Proc. Electrochem. Soc.*, **Proc. Vol. 1989–11**, 99 (1989).
21. B. C. H. Steele, P. H. Middleton, and R. A. Rudkin, *Solid State Ion.*, **40–41**, 388 (1990).
22. C. Xu, P. Gansor, J. W. Zondlo, K. Sabolsky, and E. M. Sabolsky, *J. Electrochem. Soc.*, **158**, B1405 (2011).
23. B. Mirfakhraei, S. Paulson, V. Thangadurai, and V. Birss, *J. Power Sources*, **243**, 95 (2013).
24. T. Hays, A. M. Hussain, Y. L. Huang, D. W. McOwen, and E. D. Wachsman, *ACS Appl. Energy Mater.*, **1**, 1559 (2018).
25. M. Gerstl, A. Nenning, R. Iskandar, V. Rojek-Wöckner, M. Bram, H. Hutter, and A. K. Opitz, *Materials*, **9**, 649 (2016).
26. D. R. Mullins, *Surf. Sci. Rep.*, **70**, 42 (2015).
27. D. R. Mullins and T. S. McDonald, *Surf. Sci.*, **601**, 4931 (2007).
28. S. H. Overbury, D. R. Mullins, D. R. Huntley, and L. Kundakovic, *J. Phys. Chem. B*, **103**, 11308 (1999).
29. R. Leah et al., *ECS Trans.*, **103**, 679 (2021).
30. R. Leah et al., *ECS Trans.*, **57**, 461 (2013).
31. K. T. Lee and E. D. Wachsman, *MRS Bull.*, **39**, 783 (2014).
32. I. Robinson, Y. Huang, S. A. Horlick, A. M. Hussain, A. Pesaran, and E. D. Wachsman, *ECS Trans.*, **111**, 47 (2023).
33. A. M. Abdalla, S. Hossain, A. T. Azad, P. M. I. Petra, F. Begum, S. G. Eriksson, and A. K. Azad, *Renewable Sustainable Energy Rev.*, **82**, 353 (2018).
34. S. Primdahl and M. Mogensen, *Solid State Ion.*, **152–153**, 597 (2002).
35. A. Weber, T. Dickel, and E. Ivers-Tiffée, *in Proceedings of the 12th European SOFC & SOE Forum, B0507* (2016).
36. F. Kullmann, A. Schwiers, M. Juckel, N. H. Menzler, and A. Weber, *ECS Trans.*, **111**, 1013 (2023).
37. S. Primdahl and Y. L. Liu, *J. Electrochem. Soc.*, **149**, A1466 (2002).

38. H. Kurokawa, T. Z. Sholklapper, C. P. Jacobson, L. C. De Jonghe, and S. J. Visco, *Electrochem. Solid-State Lett.*, **10**, 135 (2007).
39. J. W. Yun, S. P. Yoon, J. Han, S. Park, H. S. Kim, and S. W. Nam, *J. Electrochem. Soc.*, **157**, B1825 (2010).
40. H. Schichlein, A. C. Müller, M. Voigts, A. Krügel, and E. Ivers-Tiffée, *J. Appl. Electrochem.*, **32**, 875 (2002).
41. B. A. Boukamp, *Solid State Ion.*, **20**, 31 (1986).
42. D. Klotz, A. Weber, and E. Ivers-Tiffée, *Electrochim. Acta*, **227**, 110 (2017).
43. V. Sonn, A. Leonide, and E. Ivers-Tiffée, *J. Electrochem. Soc.*, **155**, B675 (2008).
44. A. Hagen, *J. Electrochem. Soc.*, **160**, F111 (2013).
45. H. P. He, A. Wood, D. Steedman, and M. Tilleman, *Solid State Ion.*, **179**, 1478 (2008).
46. M. Schönleber, D. Klotz, and E. Ivers-Tiffée, *Electrochim. Acta*, **131**, 20 (2014).
47. B. A. Boukamp, *J. Electrochem. Soc.*, **142**, 1885 (1995).
48. M. Riegraf, R. Costa, G. Schiller, K. A. Friedrich, S. Dierickx, and A. Weber, *J. Electrochem. Soc.*, **166**, F865 (2019).
49. C. Grosselindemann, N. Russner, S. Dierickx, F. Wankmüller, and A. Weber, *J. Electrochem. Soc.*, **168**, 124506 (2021).
50. J. Uecker, I. D. Unachukwu, V. Vibhu, I. C. Vinke, R. A. Eichel, and L. G. J. (Bert) de Haart, *Electrochim. Acta*, **452**, 142320 (2023).
51. F. Kullmann, M. Mueller, A. Lindner, S. Dierickx, E. Mueller, and A. Weber, *J. Power Sources*, **587**, 233706 (2023).
52. S. Linderoth, N. Bonanos, K. V. Jensen, and J. B. Bilde-Sørensen, *J. Am. Ceram. Soc.*, **84**, 2652 (2001).
53. A. Lefarth, B. Butz, H. Störmer, A. Utz, and D. Gerthsen, *ECS Trans.*, **35**, 1581 (2011).
54. T. Shimonosono, H. Kishimoto, M. E. Brito, K. Yamaji, T. Horita, and H. Yokokawa, *Solid State Ion.*, **225**, 69 (2012).
55. F. Kullmann, C. Grosselindemann, L. Salamon, F.-M. Fuchs, and A. Weber, *Fuel Cells*, **23**, 420 (2023).
56. A. Schwiers, C. Lenser, O. Guillon, and N. H. Menzler, *J. Eur. Ceram. Soc.*, **43**, 6189 (2023).
57. S. Wang, T. Kobayashi, M. Dokiya, and T. Hashimoto, *J. Electrochem. Soc.*, **147**, 3606 (2000).
58. R. W. Powell, R. P. Tye, and M. J. Hickman, *Int. J. Heat Mass Transf.*, **8**, 679 (1965).
59. Y. Liu, M. Juckel, N. H. Menzler, and A. Weber, *ECS Trans.*, **111**, 1855 (2023).
60. A. Tsoga, A. Naoumidis, and D. Stöver, *Solid State Ion.*, **135**, 403 (2000).
61. W. G. Bessler, M. Vogler, H. Störmer, D. Gerthsen, A. Utz, A. Weber, and E. Ivers-Tiffée, *Phys. Chem. Chem. Phys.*, **12**, 13888 (2010).
62. J. Joos, *Microstructural Characterisation, Modelling and Simulation of Solid Oxide Fuel Cell Cathodes*, Karlsruhe Insitute of Technology (2017), KIT Scientific Publishing Karlsruhe.
63. J. Szász, F. Wankmüller, V. Wilde, H. Störmer, D. Gerthsen, N. H. Menzler, and E. Ivers-Tiffée, *J. Electrochem. Soc.*, **165**, F898 (2018).
64. V. A. Rojek-Wöckner, A. K. Opitz, M. Brandner, J. Mathé, and M. Bram, *J. Power Sources*, **328**, 65 (2016).
65. M. Riegraf, R. Costa, G. Schiller, and K. A. Friedrich, *ECS Trans.*, **78**, 1285 (2017).
66. S. Uhlenbruck, N. Jordan, D. Sebold, H. P. Buchkremer, V. A. C. Haanappel, and D. Stöver, *Thin Solid Films*, **515**, 4053 (2007).
67. A. Weber, S. Dierickx, A. Kromp, and E. Ivers-Tiffée, *Fuel Cells*, **13**, 487 (2013).